Conformational plasticity across phylogenetic clusters of RND multidrug efflux pumps and its impact on substrate specificity

Mariya Lazarova[1], Thomas Eicher[1], Clara Börnsen[2], Hui Zeng[1], Mohd Athar[3], Ui Okada[4], Eiki Yamashita[5], Inga M. Spannaus[1], Max Borgosch[1], Hi-jea Cha[1], Attilio V. Vargiu[3], Satoshi Murakami[4*], Kay Diederichs[6*], Achilleas S. Frangakis[2*], Klaas M. Pos [1*]

[1] Institute of Biochemistry, Goethe-University Frankfurt, Germany

[2] Buchmann Institute for Molecular Life Sciences and Institute of Biophysics, Goethe-University Frankfurt, Germany

[3] Department of Physics, University of Cagliari, Italy

[4] Department of Life Science and Technology, Tokyo Institute of Technology, Yokohama, Japan

[5] Institute for Protein Research, Osaka University, Japan

[6] Department of Biology, University of Konstanz, Germany

Author contributions:

ML performed and analysed the sequence similarity comparison of RND efflux pumps. TE and HC established the phenotype screening pipeline for the AcrB mutants. ML and IMS performed the plate dilution assays and determined the minimal inhibitory concentration for all substrates for all technical and biological repeats. ML performed the whole cell transport assay. ML analysed all phenotype data. ML and TE expressed and purified the AcrB V612F (TE), and V612W and V612N (ML) samples for crystallisation and performed the crystallisation experiments. ML, TE and KD acquired x-ray diffraction data and built and refined the respective structural models. UO established the OqxB overexpression system. SM purified OqxB for crystallisation and performed the crystallisation experiment and EY performed the X-ray diffraction experiment. SM performed the crystallographic analysis of the OqxB_TTO structure. ML and HZ expressed and purified AcrB wildtype (HZ), and V612F and V612W (ML) samples in DDM and prepared the grids for cryo-EM analysis. ML, HC and CB acquired

33 the cryo-EM datasets and ML and CB analysed the data. ML built and refined the O state models

34 of V612F and V612W. MB established the reconstitution protocol for the samples solubilised

35 in salipro nanodiscs. ML and MB expressed and purified the AcrB wildtype (ML) and OqxB

36 (ML and MB) samples in nanodiscs and prepared the cryo-EM grids. ML acquired the cryo-

37 EM datasets, analysed the data and built and refined the OqxB structural model. ML, MA and

38 AVV prepared and performed the docking and free binding energy calculation and analysed the

39 results. ML, TE, KMP, AVV, KD and ASF were involved in the conception and design of the

40 experiments, and the analysis and interpretation of the data. KMP, ASF, SM, UO and EY are

41 holders of the grants funding the experiments. ML and KMP wrote the manuscript. All authors

42 edited the manuscript.

43 *Competing interests:*

44 The authors declare no competing interests.

45 *Funding*

2

Data availability

The crystallographic structures are available under following PDB IDs: AcrB V612W with bound minocycline: 9FE2, AcrB V612W apo: 9FE3, AcrB V612F with bound minocycline: 9FHC (raw data doi: 10.5281/zenodo.11472085), AcrB V612F, apo: 9FE4 (raw data doi: 10.15785/SBGRID/1106), AcrB V612N (TTT state): 9FHJ, AcrB V612N (LTO state): 9FHG, OqxB (TTO state): 8ZXS. The cryo-EM structure of OqxB in salipro nanodiscs is available under PDB ID 9FDZ (EMD-50334) and the monomer classes are available under EMD-50335. The cryo-EM structures of AcrB V612F and V612W monomers in the O state and the density maps for the monomer classes from the respective datasets are available under PDB ID 9FDQ/EMD-50332 (V612F in salipro nanodiscs) and PDB ID 9FDP/EMD-50331 (V612W in DDM). The density maps for the monomer classes of the remaining cryo-EM datasets are available under following EMD IDs: AcrB wildtype in DDM: EMD-50328, AcrB V612F in DDM: EMD-50329, AcrB wildtype in salipro nanodiscs: EMD-50645.

* Corresponding authors

Klaas M. Pos, pos@em.uni-frankfurt.de

Achilleas S. Frangakis, achilleas.frangakis@biophysik.org

Kay Diederichs, kay.diederichs@uni-konstanz.de

Satoshi Murakami, murakami@bio.titech.ac.jp

84   Summary

85   Antibiotic efflux plays a key role for the multidrug resistance in Gram-negative bacteria [1–3].

86   Multidrug efflux pumps of the resistance nodulation and cell division (RND) superfamily

87   function as part of cell envelope spanning systems and provide resistance to diverse antibiotics

88   [4,5]. Here, we identify two phylogenetic clusters of RND proteins with conserved binding pocket

89   residues. Based on the characterisation of one representative of each cluster, *K. pneumoniae*

90   OqxB and *E. coli* AcrB, we show that the transfer of a single conserved residue between both

91   clusters alters the resistance against a panel of structurally unrelated drugs. The substitution is

92   not only associated with changes in the binding pocket architecture, but also alters the

93   equilibrium between the conformational states of the transport cycle. We show that AcrB and

94   OqxB adopt fundamentally different apo states that suggest different mechanisms of initial

95   substrate binding and might determine the differences between the substrate preferences of both

96   pumps. The observed conformational heterogeneity between different RND clusters is

97   suggested to be phylogenetically conserved and might play a role for the diversification of the

98   resistance phenotype between homologous RND multidrug efflux pumps.

99

Introduction

Active antibiotic export greatly contributes to both intrinsic and acquired resistance in Gram-negative bacteria. While overexpression of drug efflux pumps is often associated with fitness costs, under antibiotic stress it provides an opportunity window for mechanisms of permanent resistance to evolve [1,2,6]. Resistance nodulation and cell division (RND) efflux pumps are secondary active antiporters that are ubiquitous across all domains of life. As part of tripartite multidrug efflux systems in Gram-negative bacteria, they span the entire cell envelope and export a broad variety of structurally and chemically unrelated toxic substrates [4,7]. The activity of RND efflux pumps is associated with a multidrug resistance phenotype in all clinically relevant Gram-negative bacteria [1,2,8–10].

Knowledge of the structure and function of RND efflux pumps was initially derived from *E. coli* AcrB, one of the best characterised representatives of this superfamily. AcrB forms a homotrimer in the inner membrane and associates with the pore-forming outer membrane factor TolC through the periplasmic adaptor protein AcrA (Fig S1). Two large periplasmic loops in AcrB form the substrate-binding porter domain (PD) and the funnel domain (FD). The full assembly of the tripartite system is necessary for efflux activity, while the PD determines substrate specificity. During drug efflux, AcrB undergoes a functional rotation where each of the three protomers sequentially cycles through the conformational states loose (L), tight (T) and open (O). Substrates can enter the PD through several channels and bind to the access pocket (AP) in the L state and the deep binding pocket (DBP) in the T state. The substrate is extruded through an exit channel in the O state by a closure of the binding pockets due to rigid-body movement of the porter subdomains. This movement is facilitated by proton binding in the transmembrane domain (TMD). The cycle resets via an O to L transition, where the proton is released from the TMD to the cytoplasm [4,11–15]. The groove of the DBP in AcrB is lined by hydrophobic, mostly aromatic, residues. They form an open pocket in the T state. In the O and L states, the rearrangements in the PD lead to the collapse of the DBP and a tight packing of the hydrophobic residues (Fig. S1) [11–13].

Crystallographic structures of apo and substrate-bound AcrB in the respective LLL and LTO states [11,12,16,17] suggest that AcrB adopts a LLL trimer in the absence of a substrate and a LTO trimer as the active pumping state. A saturated TTT state was proposed to be adopted, if an abundance of a substrate is present [18], and was confirmed by a cryo-EM structure in the presence of a high affinity T state binding inhibitor [19]. Recent structural studies of RND multidrug efflux pumps from other Gram-negative bacteria show that they share a common structural

133   architecture and general functional principles with AcrB [20–26]. However, the identification of
134   new trimer conformations, particularly the OOO states of AdeB from *A. baumanii* [22,23] and
135   CmeB from *C. jejuni* [21], has posed questions about the conservation of the AcrB transport model
136   in other RND pumps. Characterisation of substrate binding in AcrB and its homolog AdeB
137   allowed to rationalise the discrepancies in substrate specificity based on differences in key
138   substrate binding residues [22,27]. Here, we show that discrepancies between the global
139   conformational landscape can contribute to the differences in the substrate preferences of
140   homologous RND multidrug efflux pumps.

141

142

143 Results

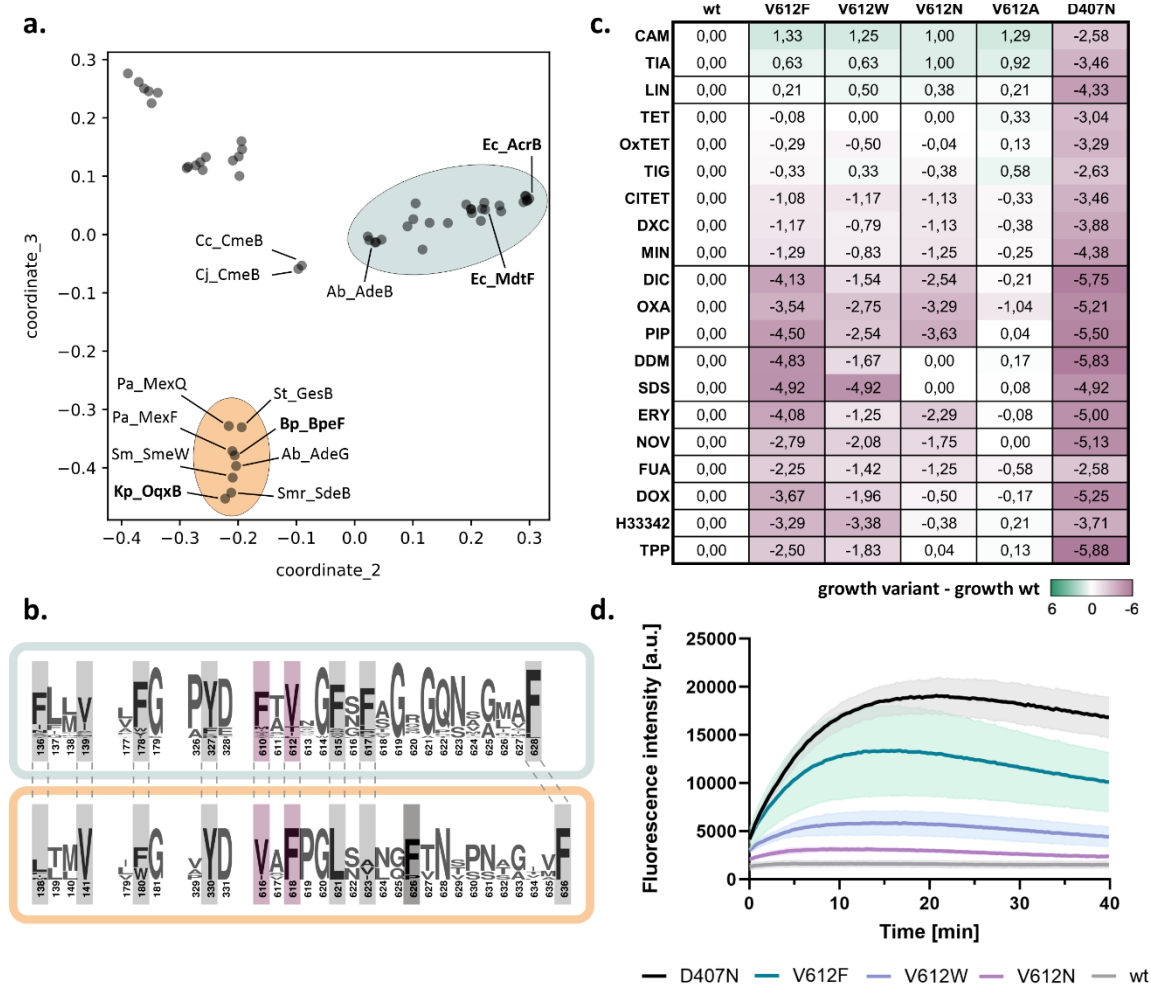144 Conserved deep binding pocket substitution alters the resistance phenotype of AcrB

145 To elucidate the conservation of DBP residues among RND efflux pumps, we analysed the
146 sequences of over 50 RND representatives from Gram-negative pathogens (table S1). Based on
147 the similarity of the full-length sequences, five phylogenetic clusters were identified (Fig. 1a
148 and S2). In two of these, hereafter referred to as AcrB and OqxB clusters, the residues defining
149 the DBP, with exception of I277 and I626, are highly conserved (Fig. 1b). The first cluster
150 includes AcrB and its closely related homolog MdtF, both from *Escherichia coli*, while the
151 second cluster includes OqxB from *Klebsiella pneumonaie* and BpeF from *Burkholderia*
152 *pseudomallei*, among others. Despite the conservation within the DBP, positions F610 and
153 V612 in the members of the AcrB cluster are exchanged in the members of the OqxB cluster
154 (Fig. 1b).

155 The V612F exchange caught our attention as a previous evolutionary study [28] demonstrated that
156 under antibiotic pressure MdtF from the AcrB cluster naturally acquires this substitution. This
157 results in an increased resistance to linezolid, tetracycline, chloramphenicol, and
158 fluoroquinolones, but a reduced resistance to macrolides [28]. Interestingly, the resistance profile
159 of this MdtF variant mirrors that of the OqxB cluster representatives, i.e. OqxB, BpeF, AdeG,
160 and MexF, which confer resistance to tetracyclines, chloramphenicol, and fluoroquinolones, but
161 not macrolides [24,25,29–31].

162 To elucidate the role of the DBP residue at position 612 in substrate binding and transport, we
163 substituted V612 in AcrB with F to mimic the sequence in the OqxB cluster and with a
164 physicochemical similar (W) and different (N, A) residues. We tested the resistance phenotypes
165 of wildtype AcrB and the V612 variants against a panel of 20 toxic substrates (Fig. 1c and S3).
166 All V612 variants showed a small but highly reproducible increase in resistance towards
167 phenicols and linezolid, in line with the phenotype of the MdtF variant and the members of the
168 OqxB cluster [24,25,28–31]. However, resistance for most other tested substrates was decreased for
169 the V612F/W variants, with V612F having a more pronounced phenotype. V612N also showed
170 a similar reduced resistance for many of the tested drugs (Fig. 1c).

171 To directly assess AcrB-mediated efflux, we performed a whole cell drug transport assay with
172 the fluorescent dye berberine (Fig. 1d). Berberine accumulation inside *E. coli* cells can be
173 monitored by the increase of fluorescence due to its DNA-intercalating properties. AcrB-TolC
174 effectively exports berberine resulting in a much lower fluorescence signal compared to efflux-

175 deficient cells. In agreement with the phenotype assays (Fig. 1c) that suggest compromised

176 activity for the V612 variants, a reduction of berberine efflux was observed (Fig. 1d). Of the

177 tested V612 variants, V612F was most and V612N the least compromised in berberine efflux,

178 compared to cells expressing wildtype AcrB.

	wt	V612F	V612W	V612N	V612A	D407N
CAM	0,00	1,33	1,25	1,00	1,29	-2,58
TIA	0,00	0,63	0,63	1,00	0,92	-3,46
LIN	0,00	0,21	0,50	0,38	0,21	-4,33
TET	0,00	-0,08	0,00	0,00	0,33	-3,04
OxTET	0,00	-0,29	-0,50	-0,04	0,13	-3,29
TIG	0,00	-0,33	0,33	-0,38	0,58	-2,63
CITET	0,00	-1,08	-1,17	-1,13	-0,33	-3,46
DXC	0,00	-1,17	-0,79	-1,13	-0,38	-3,88
MIN	0,00	-1,29	-0,83	-1,25	-0,25	-4,38
DIC	0,00	-4,13	-1,54	-2,54	-0,21	-5,75
OXA	0,00	-3,54	-2,75	-3,29	-1,04	-5,21
PIP	0,00	-4,50	-2,54	-3,63	0,04	-5,50
DDM	0,00	-4,83	-1,67	0,00	0,17	-5,83
SDS	0,00	-4,92	-4,92	0,00	0,08	-4,92
ERY	0,00	-4,08	-1,25	-2,29	-0,08	-5,00
NOV	0,00	-2,79	-2,08	-1,75	0,00	-5,13
FUA	0,00	-2,25	-1,42	-1,25	-0,58	-2,58
DOX	0,00	-3,67	-1,96	-0,50	-0,17	-5,25
H33342	0,00	-3,29	-3,38	-0,38	0,21	-3,71
TPP	0,00	-2,50	-1,83	0,04	0,13	-5,88

growth variant - growth wt   6   0   -6

Figure 1: A conserved DBP residue alters the resistance phenotype conferred by *E. coli* AcrB. a. Map of pairwise sequence similarities between representative RND proteins (table S1) was generated with the multidimensional scaling pipeline PaSiMap [32]. The coordinates for the two highest dimensions (coordinate_2 and coordinate_3) are displayed in the plot. The AcrB and OqxB clusters are highlighted in cyan and orange, respectively. Abbreviations are given in figure S2. b. Consensus sequence of the AcrB (cyan) and OqxB (orange) clusters. Residues that are part of the DBP are highlighted. Residue numbers correspond to the sequence of AcrB or OqxB, respectively. F617 of the AcrB cluster is poorly conserved in the OqxB cluster. This is likely compensated by F626 (darker grey) that adopts similar position in the OqxB structure (see Fig. 2a). F610 and V612 (purple) of the AcrB cluster have exchanged positions in the OqxB cluster. c. Phenotype characterisation of AcrB V612 variants by plate dilution assays. A serial dilution of the bacterial culture was applied on plates containing different toxic substrates. The last dilution step for which growth was detected was determined and normalised to the wildtype (wt). The inactive D407N was used as a negative control. Green: increased growth, purple: decreased growth; abbreviation as in table S2. The figure shows average data of three biological replicates. The original images of the plate dilution assays

193   are available under source data. d. Berberine accumulation in *E. coli* cells expressing different AcrB V612 variants.

194   AcrB activity was monitored by measurement of the berberine fluorescence. AcrB wildtype (wt) and the inactive

195   D407N were used as controls. Data present the mean values (solid line) with standard deviation (shaded

196   background) of three biological replicates.

197

198   Structural characterisation of antibiotic binding to AcrB V612 variants

199   The DBP residues are directly involved in substrate binding as was shown for AcrB and further

200   RND efflux pumps [12,13,22,23,25]. Thus, the various V612 substitutions alter the substrate binding

201   site, and the observed phenotype change in the AcrB variants may be explained through

202   changed ligand interactions. To assess this, we solved co-structures of V612F and V612W in

203   complex with minocycline via X-ray crystallography. In contrast to the minocycline structure

204   of AcrB wildtype, that displays an asymmetric LTO with bound minocycline in the T state

205   protomer [12,13], the obtained V612F and V612W co-structures are in the C3 symmetric space

206   group I23 with one AcrB monomer and one DARPin molecule in the asymmetric unit. Thus,

207   the structures represent an AcrB trimer with three identical chains closely fitting the T state of

208   wildtype AcrB (RMSD 1.1 Å for V612F and 1.1 Å for V612W, wildtype reference PDB ID:

209   4dx5) (Fig. 2a and Fig. S4a). The introduced F or W side chain is sandwiched between the

210   reoriented F615 and F610, forming a stack of aromatic rings, and closes off the groove of the

211   DBP, thus reducing its size. Minocycline is shifted in the binding pocket (Fig. 2b) to avoid steric

212   overlap with the introduced F or W at position 612. Compared to the wildtype co-structure, the

213   contact between R620 and minocycline is lost, but appears to be compensated by additional H-

214   bonding interactions (Fig. 2c and S4c). Further, the flipped F615 is in interaction distance of

215   the aromatic ring of minocycline. The V612 variant co-structures demonstrate the plasticity of

216   the DBP that is able to accommodate the ligand and allows the formation of alternative

217   interactions despite the alterations in the binding network. Corresponding to these results, the

218   resistance against minocycline is only marginally affected by the V612 substitutions (Fig. 1c)

9
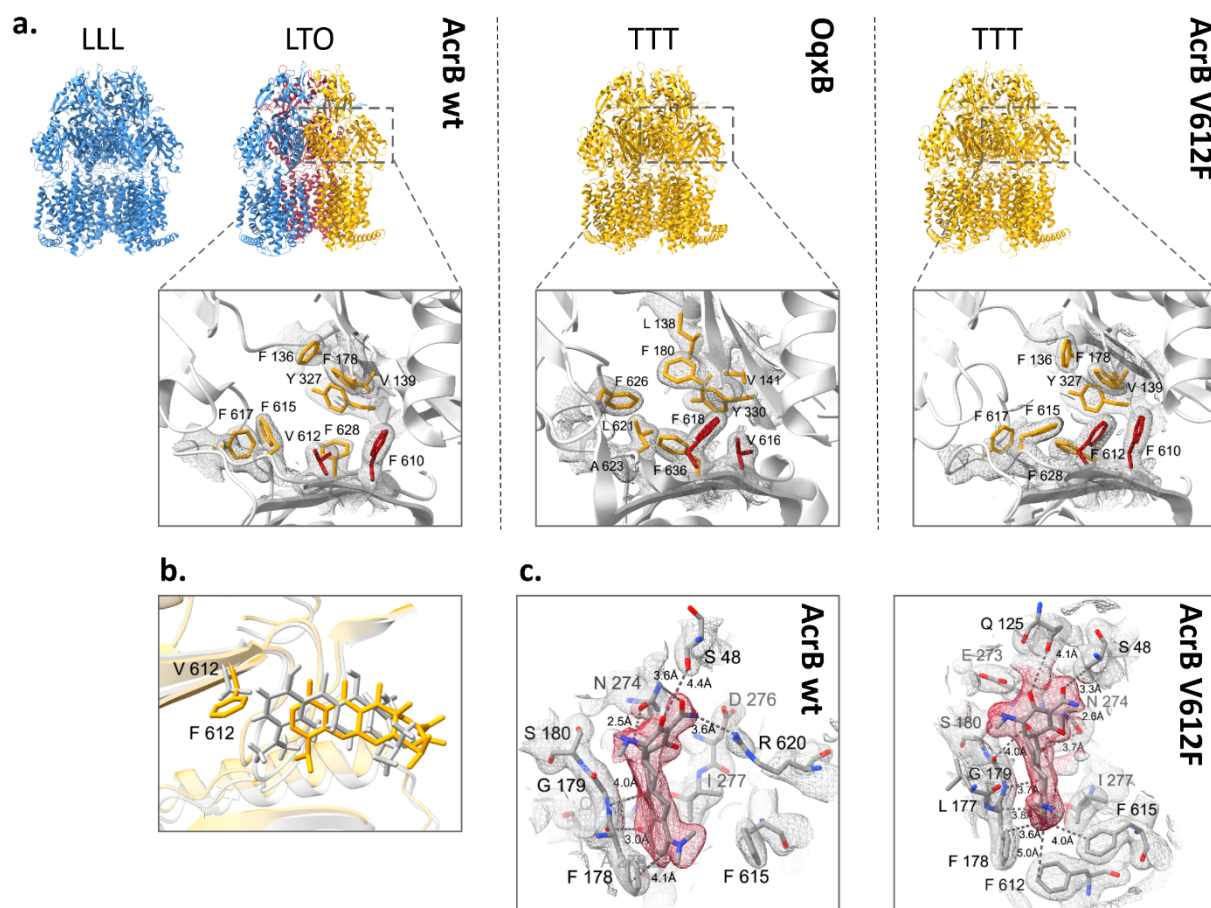
Figure 2: Comparison of the deep binding pocket of AcrB wildtype, AcrB V612F and OqxB. a. Upper panel: Side view of the trimer structures of AcrB, OqxB, and AcrB V612F with each monomer coloured corresponding to the conformational state (L state in blue, T state in yellow and O state in red). The AcrB wildtype (left) has been crystallised in the LLL and LTO states (PDB ID: 1iwg and 4dx5, respectively) whereas OqxB (middle) has been crystallised in the TTT state (PDB ID: 7cz9). Here we show that both AcrB V612F (right) and V612W (Fig. S4) crystallise in the TTT state. Lower panel: top view of the deep binding pocket in the T state with conserved deep binding pocket residues shown as sticks. Crystallographic 2Fo-Fc densities are depicted as a mesh contoured at 1 σ. The residues at positions 610 and 612 in AcrB and the corresponding positions 616 and 618 in OqxB are highlighted in red. b. Overlay of the minocycline binding pose in the experimental structures of AcrB wildtype (grey, PDB ID: 4dx5) and V612F (yellow). The residue at position 612 is shown as sticks. c. Minocycline interactions in the deep binding pocket of AcrB wildtype (PDB ID: 4dx5) and V612F. The crystallographic 2Fo-Fc maps are shown at σ 1 (mesh) and the densities for minocycline are highlighted in red. Minocycline and residues with at least one atom within 4 Å distance of the ligand are shown as sticks and indicated with single letter amino acid code and position number. The interaction (dashed lines) and distances between the side chains and minocycline are indicated. Carbon atoms are given in grey, oxygen in red, and nitrogen in blue.

To assess changes in the DBP interactions with further substrates, we performed a computational study that is discussed in detail in the supplementary information. In brief, the results indicate that the V612F and V612W substitutions alter the binding poses of chloramphenicol and doxorubicin. These changes are likely provoked by the alteration of the

10

DBP architecture and the interactions with the newly introduced aromatic residue and might be the reason behind the observed change in the phenotype (Fig. S5, Table S4, Supplementary information). However, the binding pose, the interactions, and the calculated free binding energies for the macrolide erythromycin were similar for AcrB wildtype and variants. Erythromycin is a high molecular weight drug that binds in the AP-DBP-interface of the L state in *E. coli* AcrB [33]. In the close homolog AcrB from *K. pneumoniae* (96 % sequence similarity), erythromycin binding in the DBP of the T state has also been described [34]. Erythromycin likely forms initial interactions with the AP of the L state and is transferred to the PD interior during the L to T state transition. Thus, the initial binding of erythromycin in the L protomer appears to be a prerequisite for its transport.

In contrast to wildtype AcrB, that crystallises in the LLL and LTO states [11–13,16,33,35], the V612F/W crystal structures were exclusively obtained in the TTT state (Fig. 2, S4). We thus hypothesized that the substitution impedes the formation of the L state and this in turn might play a role for the transport of L state-binding drugs such as erythromycin. The TTT conformation has previously been shown for AcrB wildtype in a single-particle cryogenic electron microscopy (cryo-EM) structure of the AcrAB-TolC complex with the high affinity inhibitor MBX3132 in the DBP of all three T protomers [19]. As we anticipated that minocycline binding to the DBP might be a driver for the TTT conformation in the V612 variants, we solved the apo structures by X-ray crystallography. These also adopted the TTT state with an open, but empty DBP. Further, two apo-TTT state crystal structures of representatives from the OqxB cluster, BpeF and OqxB have been described recently [24,25]. The structures of these detergent-solubilized proteins indicated the presence of detergent densities inside the DBP and detergent binding was proposed to induce the observed TTT state [24,25]. Despite the high resolution of our AcrB V612F/W electron density maps (2.3 Å and 2.8 Å, respectively), no clearly assignable detergent (DDM) densities could be observed in the DBP. We therefore assumed that the crystallisation conditions might favour the crystal contacts leading to the TTT state for the AcrB variants. To elucidate the conformation of AcrB without the crystallisation bias, we assessed the structure of the variants by cryo-EM.

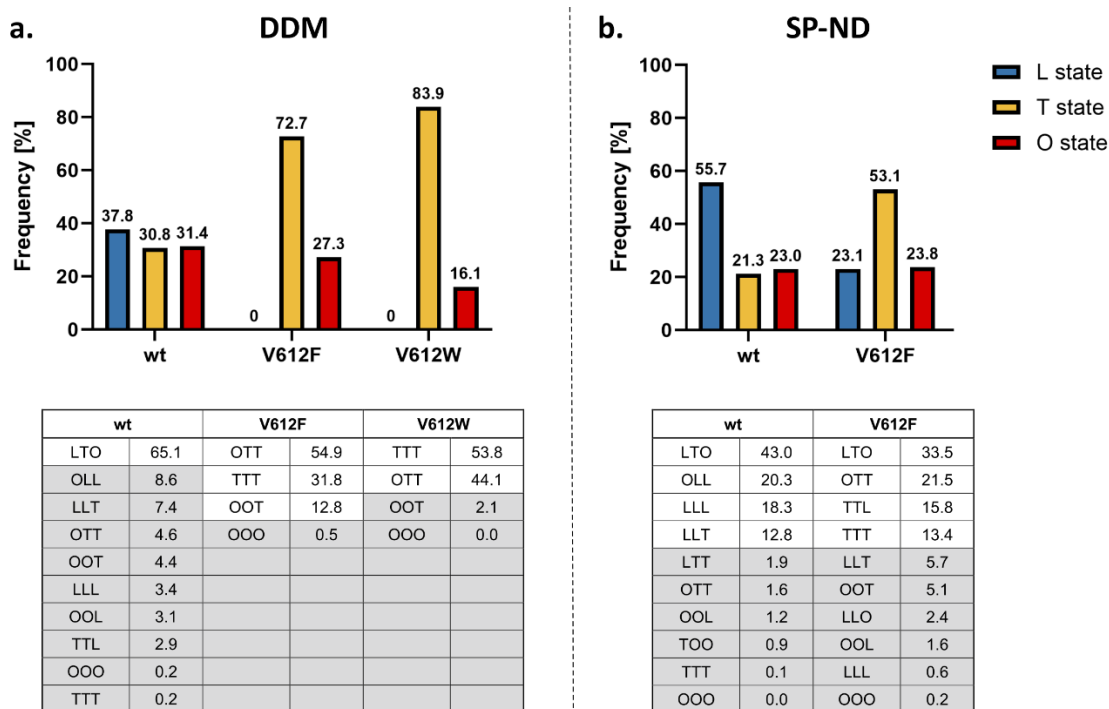Distribution of conformational states in AcrB wildtype, V612F and V612W

The trimeric states and the distribution of the monomeric conformations of AcrB wildtype and the V612F/W variants were determined via cryo-EM both in a DDM-solubilized and in detergent-free SaliPro nanodisc (SP-ND) [36] reconstituted samples (Fig. S6-S12). For AcrB

11

272   wildtype solubilised in DDM, an almost even distribution of particles in the L, T and O state

273   was observed with most of the trimers (65.1 %) in the LTO state (Fig. 3a). This is in agreement

274   with the LTO apo-state structures observed by X-ray crystallography [11,12,17]. In contrast, V612F

275   and V612W mainly showed particles in the T state (72.7 % and 83.9 %, respectively), with

276   these variants displaying trimers predominantly in the TTO (54.9 % V612F, 44.1 % V612W)

277   and TTT (31.8 % V612F, 53.8 % V612W) states (Fig. 3a). Notably, no particles in the L state

278   were found for V612F/W.

279   For wildtype AcrB in SP-ND, a higher abundance of the L state was observed compared to the

280   DDM sample (55.7 % in SP-ND versus 37.8 % in DDM) (Fig. 3). Further, the number of trimer

281   particles in the LTO state (43.0 %) decreased, while the abundance of LLO, LLL and LLT states

282   was higher. This suggests an intrinsic flexibility of the AcrB trimer that exists in a dynamic

283   equilibrium between the different conformational states. DDM binding seems to increase the

284   number of T states driving the LTO formation from the LLO, LLL and LLT trimers. DDM was

285   not detected in the DBP, however well-resolved detergent densities were present in the

286   TM1/TM2 groove in the TMD (Fig. S15a-b). DDM binding in this groove has been observed

287   in several crystallographic structures of AcrB [13,35] and the TM1/TM2 groove might represent

288   an allosteric binding site or a pocket for initial binding at the entrance of channel 4. In the T

289   state, the PN2 subdomain shifts closer to the membrane plane in comparison to the L state

290   (Fig. S15c) and allows interactions of the maltoside headgroup of DDM with the residues N298

291   and D301. This is specific to the T state since in the L state the PN2 subdomain is in the up

292   conformation and N298 and D301 are not within hydrogen bonding distance of the DDM. Thus,

293   the interactions of DDM in the TM1/TM2 groove might stabilise PN2 architecture of the T state

294   and facilitate the increased formation of T monomers.

295   For V612F in SP-ND we found that all three states, L, T and O, were present (Fig. 3b) indicating

296   that DDM binding is responsible for the absence of the L state in the detergent-solubilised

297   samples. The T state remains, however, the most abundant state for V612F (53.1 % T state in

298   V612F in SP-ND vs 21.3 % in the wildtype). The trimer adopts the LTO state, and also the

299   TTO, TTT and TTL states in contrast to the LLO, LLL and LLT states observed for wildtype

300   AcrB. Thus, the introduced substitution clearly shifts the equilibrium between the L and T states

301   in favour of the T state. F/W612 appears to stabilise an open DBP even in the absence of a

302   substrate, as the bulky side chain might mimic binding of a small substrate. Moreover, the

303   proximity of the bulky aromatic sidechains in the hydrophobic cluster might introduce a steric

304   hindrance for the rearrangements associated with the closing of the DBP required for the O and

305   L state formations. Indeed, our structural models of the best resolved O monomer densities

306   show that the DBP remains partially open in V612F/W structure (Fig. S16). We assume that the

307   O state conformation is still feasible due to compensating interactions, such as the PC1 and PC2

308   subdomain proximity, and PN1 subdomain interaction with the neighbouring protomer.

309   However, in the L state such stabilizing contacts are far less pronounced. Thus, the stabilisation

310   of the T state DBP in its open form and impaired DBP closing are likely the reason behind the

311   observed increased abundance of the T state on expense of the L state in the V612F variant.

312   Detergent binding to the TM1/TM2 groove likely potentiates the shift toward the T state,

313   resulting in the complete absence of the L state in the DDM solubilised samples.

a. DDM

wt		V612F		V612W	
LTO	65.1	OTT	54.9	TTT	53.8
OLL	8.6	TTT	31.8	OTT	44.1
LLT	7.4	OOT	12.8	OOT	2.1
OTT	4.6	OOO	0.5	OOO	0.0
OOT	4.4				
LLL	3.4				
OOL	3.1				
TTL	2.9				
OOO	0.2				
TTT	0.2				

b. SP-ND

wt		V612F	
LTO	43.0	LTO	33.5
OLL	20.3	OTT	21.5
LLL	18.3	TTL	15.8
LLT	12.8	TTT	13.4
LTT	1.9	LLT	5.7
OTT	1.6	OOT	5.1
OOL	1.2	LLO	2.4
TOO	0.9	OOL	1.6
TTT	0.1	LLL	0.6
OOO	0.0	OOO	0.2

314

Figure 3: Cryogenic electron microscopy (cryo-EM) analysis of the conformational states of AcrB. Cryo-EM datasets of AcrB wildtype (wt), V612F and V612W were acquired and the number of particles in the L, T and O conformations was determined as described in Fig. S6. The evaluation of each dataset is shown in more detail in Fig. S7-12. Summary data for the frequency of each monomer state in the samples of AcrB solubilised in DDM (a) and reconstituted in salipro nanodiscs (b) are shown in the top panel. The distribution of trimeric states is shown in the bottom panel. The frequency is presented as the percentage of the total number of particles.

321   For the V612W variant a similar structural effect is expected as for V612F due to the

322   introduction of a bulky aromatic side chain in the DBP, corresponding to the TTT crystal

323   structure that was obtained for both V612F and V612W. For the V612N variant we obtained

324   two crystal structures in different space groups, which represent not only the TTT conformation,

325   but also the LTO conformation as seen in wildtype AcrB (Fig. S17-18). Presumably here the

326   closing of the DBP in the L state is also unfavourable due to the introduction of the hydrophilic

13

asparagine within the aromatic cluster. This is likely less drastic than the effect of the V612F/W substitutions but could still shift the equilibrium between the L and T states, hence crystal structures were obtained in both LTO and TTT conformations. The reduction of the abundance of the L state likely affects the transport of substrates that require initial binding in the L protomer, such as erythromycin. Thus, the change of the global conformation of AcrB represents an additional effect of the substitution beyond the direct interactions in the DBP. The observed changes in the phenotype are likely provoked by an interplay of an altered interaction network and a change in the initial binding and entry of the substrate.

CryoEM structure of *K. pneumoniae* OqxB

Given the parallels in both the phenotype and the structural characteristics of AcrB V612F and the proteins from the OqxB cluster, we decided to assess the structural characteristics of OqxB as a representative of this cluster. We were able to obtain a detergent solubilised OqxB crystal structure in the TTO state (table S5, figure S19). Thus, OqxB can also adopt an asymmetric structure next to the previously determined TTT state [25] in the presence of a substrate (here: DDM). The O monomer of the TTO structure closely resembles the O state of AcrB and has an open exit channel for substrate extrusion as expected (Fig. 4c, table S5). Further, we reconstituted OqxB in SP-ND to assess its distribution of conformational states in a detergent free environment with cryo-EM (Fig. S13). In contrast to all AcrB samples, that contained a mixture of several trimeric states, OqxB showed a homogeneous structure with all particle classes representing the same state (Fig. S13). Based on the electron density map of the OqxB trimer, a structural model was built with 2.8 Å global resolution (Fig. S14). The three individual protomers in the OqxB trimer adopt a highly similar conformation with an all-atom RMSD between the individual chains of ≤ 0.8. In comparison to the T state (reference OqxB_TTT PDB ID: 7cz9), each protomer chain displays an upward shift of the transmembrane helix 2 (TM2) and a tight packing of the subdomains within the PD (Fig. 4a). Further, the central K946 residue of the proton translocation network within the TMD is flipped towards N947 and thus oriented away from both titratable residues D411 and D410 (Fig. 4b). These are characteristics of the O state [4] that were also observed for the O monomer of the crystallographic TTO structure (Fig. S19). Therefore, the SP-ND reconstituted OqxB trimer resembles the OOO states observed for AdeB and CmeB [21,22] more closely than the flexible asymmetric AcrB states. However, in all three monomers of OqxB all channels leading to the PD including the exit tunnel are very narrow throughout their entire length with a bottleneck radius between 1.1 Å and 1.5 Å (Fig.

14

360   4c). These channels are too narrow to fit any known OqxB substrate. Thus, the cryo-EM

361   structure of OqxB has the typical architecture of the O state, but with a closed exit tunnel and

362   will hereafter be referred to as O*O*O* state. In contrast to the O state observed in the

363   crystallographic TTO structure, the O* state of OqxB has a pronounced shift in the PN1

364   subdomain (figure S20) which is likely the reason for the closed configuration of the exit

365   channel.

366   A monomer state with the characteristic architecture of the O state but with a closed exit channel

367   has been described for several further HAE-1 RND efflux pumps: *B. pseudomallei* BpeB,

368   *C. jejuni* CmeB, *A. baumannii* AdeB and *P. aeruginosa* MexB [21,23,24,26]. A comparison between

369   the different O* states reveals that for BpeB, AdeB and MexB a shift of the PN1 subdomain is

370   observed in the O* state in comparison to the O state similarly to OqxB (Fig. S20). This PN1

371   orientation resembles the conformation of this subdomain in the T state and is likely the reason

372   for the reduced diameter of the exit channel. It has been proposed that the O* state is formed

373   during the transition from O to L [24] and the following model, incorporating the O* state in the

374   conformational cycle, is feasible: substrates enter the PD through different channels or through

375   the AP and ultimately reach the DBP in the T state. Protonation in the TMD results in the

376   formation of the O state and extrusion of the substrate through the exit channel as previously

377   described [11,12,14]. The presence of the substrate might stabilise the open conformation of the exit

378   channel in the O state. Next, the exit channel presumably closes to prevent backsliding of the

379   substrate, while the titratable residues of the TMD remain protonated – the O* state is formed.

380   The closing of the exit channel is likely facilitated by the neighbouring monomer adopting the

381   O state, since a computational study suggests that the presence of two neighbouring O states

382   results in a steric overlap in the PD [14] that likely occurs between the PN1 subdomain of one

383   monomer and PN2 subdomain of its neighbour. Alternatively, the exit tunnel might

384   spontaneously collapse after the substrate has left the channel. From the O* state the proton is

385   released on the cytoplasmic side of the membrane, and deprotonation of the titratable residues

386   in the TMD triggers the structural changes that lead to the L state as previously described [11,12,14].

387   The O* state might represent a local energy minimum in the OqxB structure which leads to the

388   formation of O*O*O* in the absence of a substrate.

389
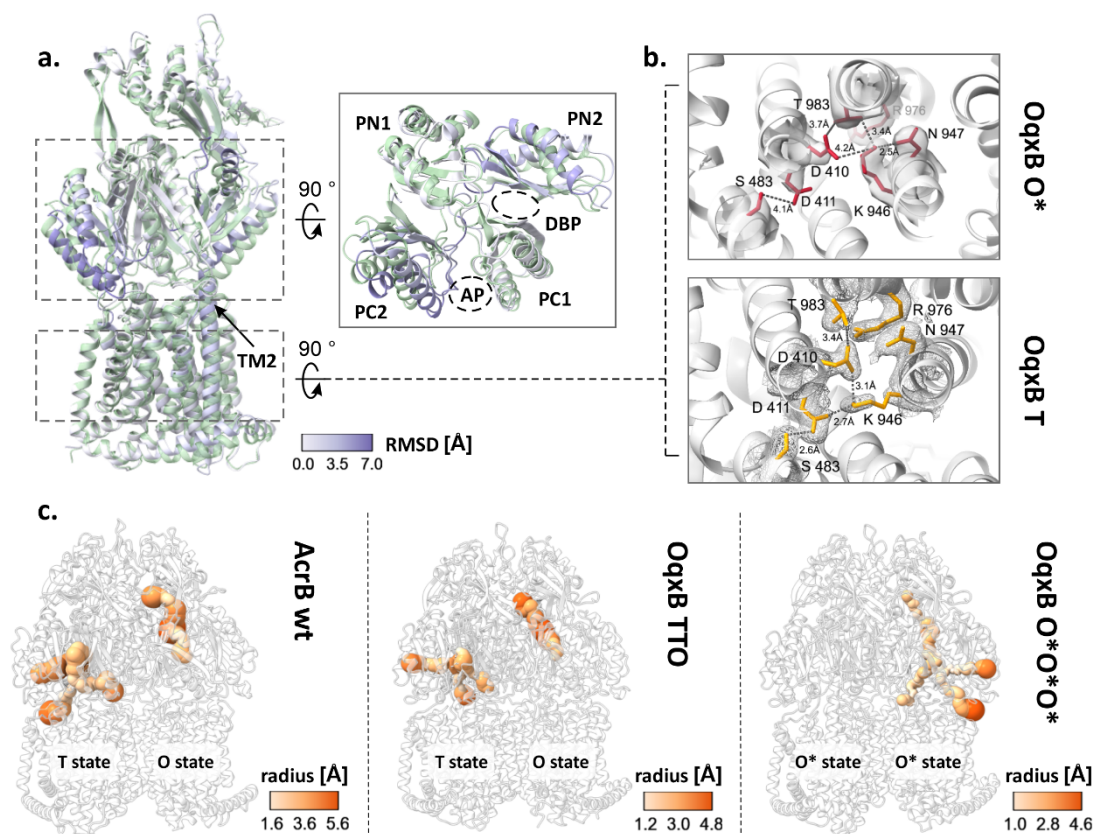
Figure 4: Cryogenic electron microscopy (cryo-EM) structure of OqxB reconstituted in salipro nanodiscs. a-b. Comparison of the OqxB structure in the O* and T states. The O*O*O* cryo-EM structure of OqxB presented in this study was overlayed with the previously solved crystallographic OqxB structure in the TTT state (PDB ID: 7cz9). One monomer of each structure is shown representatively in a. The O* state is coloured by the RSMD between both structures, the T state is coloured green. Left panel – overall structure of the monomer, right inlet: top view of the porter domain. The transmembrane helix 2 (TM2) and the subdomains of the porter domain with the access and deep binding pockets (AP and DBP) are highlighted. b. Proton translocation network in the OqxB O* (top, red) and T (bottom, yellow) states. Crystallographic 2Fo-Fc maps (T state, PDB ID: 7cz9) are depicted at σ 1 (mesh). Cryo-EM densities (O* state) are depicted at contour level 0.238 (solid surface). c. Entry and exit channels in the AcrB and OqxB structures. The channels in the porter domain of the LTO AcrB structure (left panel, PDB ID: 4dx5), the crystallographic structure of OqxB in the TTO state (middle panel, this study) and of the cryo-EM O*O*O* structure of OqxB (right panel, this study) were calculated with MOLE [37]. The channels are shown coloured by radius according to the respective colour key.

16

Discussion

Members of the OqxB cluster share similar resistance phenotype [24,25,29–31] and their substrate preferences could be partially recreated in MdtF [28] and AcrB (this study) by a single V to F substitution in the DBP. Some of the effects of this substitution on the architecture of the DBP are likely shared between members of the OqxB cluster and the MdtF and AcrB variants. These comprise the presence of an additional aromatic residue for π-π-interactions, and the reduced size of the DBP preventing the entry of the substrate deeper into the pocket. These changes alter the substrate interactions within the DBP and thus the binding and transport. Further, a comparison of the porter domain of AcrB and OqxB shows, that in the T states a shift of the PC2 subdomain towards the PC1 subdomain is observed in OqxB (Fig. S21). As these subdomains flank the AP, this results in a smaller AP cleft in OqxB compared to AcrB. Additionally, the channels leading from the TMD to the DBP in OqxB have smaller bottleneck radii and are overall narrower compared to AcrB. A constriction of the channel connecting the AP and the DBP is also observed (Fig. 4c). Finally, in sharp contrast to AcrB that adopts different conformations with at least one L state monomer in the apo state, OqxB adopts the closed O* state. Currently there is no experimental structure of OqxB in the L state, and it is unclear whether the protein can adopt this conformation. The generally narrower binding pockets and entrance channels of OqxB potentially limit the binding of high-molecular weight drugs, such as erythromycin, and thus evoke the substrate preference towards smaller and more flexible drugs, such as the phenicols, fluoroquinolones and linezolid. High-molecular weight drugs are found associated with the L state in AcrB and initial binding to this state might be an important prerequisite for their entry in the PD interior [38]. Thus, some of the phenotype similarities between members of the OqxB cluster and the V612 variants of AcrB, like the reduced resistance against erythromycin, might be induced by a common effect of reduced initial binding of high-molecular weight drugs. In OqxB this is evoked by the narrow binding pockets and entrance channels, and potentially by the absence of a L state, whereas in the AcrB variants it is induced by the decrease of the fraction of monomers in the L state.

The data presented here for AcrB and OqxB, as well as previously published structural data [20,22–25,39] reveal a striking diversity in the conformations adopted by RND multidrug efflux pumps (Fig. S22). On one side of the spectrum, AcrB adopts multiple trimer conformations in the apo state with an abundance of L monomers. Binding of a substrate to the already present open binding pockets likely changes the equilibrium between these conformations and thus favours the formation of the LTO state. On the other side of the spectrum, OqxB adopts a single

439   trimer conformation, the O*O*O* state, in which all binding pockets and entrance channels are

440   closed. Substrates might interact with the entrance cleft of the AP, inducing the opening of the

441   AP, or they might enter the PD from grooves in the TMD inducing the opening of the entrance

442   channels and binding pockets in the PD interior. Thus, the different conformational landscape

443   of AcrB and OqxB suggest two different mechanisms of initial substrate binding, a selection of

444   one out of several conformations in equilibrium for AcrB and an induced fit upon substrate

445   binding in OqxB. The RND efflux pumps CmeB from *C. jejuni* and AdeB from *A. baumanii*,

446   that bridge the AcrB and OqxB clusters show less conformational heterogeneity than AcrB and

447   adopt the OOO state that is similar to the O*O*O* state of OqxB [21–23,39]. Nevertheless, they

448   still adopt asymmetric conformations with monomers containing open substrate binding

449   pockets in the apo state (Fig. S22). The sequence features underlying the apo state configuration

450   and thus the mechanism of substrate binding might be conserved in phylogenetic clusters and

451   shared between close RND homologs. As demonstrated in the current work, changes in the

452   conformational landscape contribute to changes in the substrate specificity. Thus, the observed

453   differences between the conformational landscape of RND multidrug efflux pumps might be

454   one of the determinants of their substrate specificity spectrum.

455 Methods

456 Phylogenetic analysis of RND genes

457 For analysis of the conservation of deep binding pocket residues in a panel of Gram-negative

458 bacteria, the representative protein sequences of the HAE-1 RND transporter family in the

459 transporter classification database [40] (accessed 18.08.2023) with addition of the BpeF and

460 CmeB sequences were analysed (table S1). A phylogenetic tree was created after a multiple

461 sequence alignment with ClustalOmega [41] and visualised with iTOL [42]. Logo representations of

462 the consensus sequence of the phylogenetic clusters were created with WebLogo [43].

463 Additionally, the same set of sequences was analysed by cc-analysis after a pairwise sequence

464 alignment with PaSiMap [32].

465 Plasmids and sequences

466 *E. coli* AcrB and *K. pneumoniae* OqxB with C-terminal 6x-His-tag were expressed from the

467 pET24 vector. AcrB-specific DARPin, clone 1108_19, with a N-terminal 6x-His-Tag, and

468 saposinA with a N-terminal 6x-His-tag followed by a TEV cleavage site were expressed from

469 the pQE and pNIC28-Bsa4 vectors respectively. All constructs have been described previously

470 [17,36,44 25].

471 Bacterial strains and growth media

472 Phenotype characterisation was performed with an *E. coli* BW25113 Δ*acrB* strain. For

473 expression of AcrB and OqxB, *E. coli* C43 (DE3) Δ*acrB* cells were used. For expression of

474 DARPin *E. coli* XL1 Blue and for expression of saposinA *E. coli* Rosetta gami-2 (DE3) cells

475 were used. For vector amplification and cloning purposes *E. coli* Mach1T1 cells were used.

476 Cells were grown on LB agar plates (10 g/L tryptone, 5 g/L yeast extract, 10 g/L NaCl, 1.5 %

477 agar) or in liquid cultures in LB (10 g/L tryptone, 5 g/L yeast extract, 10 g/L NaCl) or TB (12

478 g/L tryptone, 24 g/L yeast extract, 2.31 g/l KH_2PO_4, 12.5 g/l K_2HPO_4, 0.4 % (v/v) glycerol)

479 medium containing an appropriate selection antibiotic (50 μg/mL kanamycin for pET24, 50

480 μg/mL carbenicillin for pQE, 50 μg/mL kanamycin and 34 μg/mL chloramphenicol for

481 pNIC28-Bsa4).

482 Plate dilution assays (PDA)

483 Chemically competent *E. coli* BW25113 Δ*acrB* cells were transformed with AcrB variants and

484 cultured overnight at 37 °C on LB agar plates supplemented with 50 μg/mL kanamycin. Pre-

485 cultures in LB medium with 50 μg/mL kanamycin were inoculated with a single clone and

19

486   incubated overnight at 37 °C. A serial dilution of the overnight culture starting from OD_{600} 1 to

487   OD_{600} 10^{-5} in 10-fold steps was prepared. The dilution series were spotted on LB agar plates

488   containing selection antibiotic (50 µg/mL kanamycin) and an appropriate amount of the

489   substrate of interest (table S2). Plates were incubated at 37 °C for 18 h before imaging. The

490   assay was performed with at least three biological replicates. For each experiment a control

491   plate without a substrate was prepared to ensure that all variants show equal growth in the

492   absence of the substrate. The expression levels of all variants were validated by Western blot.

493   For quantification of the results, the last dilution step for which growth was visible was

494   averaged for all replicates and normalised to the wildtype (variant – wildtype).

Minimal inhibitory concentration (MIC) determination

496   Overnight cultures of *E. coli* BW25113 Δ*acrB* cells transformed with AcrB variants were

497   prepared as described for the PDA and diluted to OD_{600} of 0.018. A serial dilution of the

498   substrate of interest in twofold dilution steps was prepared in LB medium with 50 µg/mL

499   kanamycin in a 96-well plate. 50 µL of the cell suspension was added to 100 µL of the serial

500   dilution. The plates were incubated for 18 h at 37 °C. The OD_{600} absorption of the plate was

501   determined at a plate reader before (background absorption) and after the incubation at 37 °C.

502   Background corrected OD_{600} values higher than 0.18 were defined as growth and the MIC

503   values corresponded to the lowest concentration of the substrate for which no growth was

504   detected after the 18 h incubation. The MIC determination was performed in at least biological

505   triplicates. MIC values were averaged for all replicates and normalised to the wildtype

506   ($MIC_{variant}/MIC_{wildtype}$).

Whole cell accumulation assay

508   Overnight cultures of *E. coli* BW25113 Δ*acrB* cells transformed with AcrB variants were

509   prepared as described for the PDA. 50 mL LB medium with 50 µg/mL kanamycin were

510   inoculated with 500 µL overnight culture and incubated at 37 °C until OD_{600} values of 0.7-0.9

511   were reached. Cells were harvested by centrifugation at 4000 g and 4 °C for 5 min and washed

512   with potassium phosphate (KPi) buffer (50 mM potassium phosphate pH 7.5, 1 mM $MgSO_4$).

513   Cells were resuspended in KPi buffer supplemented with 0.2 % glucose and the OD_{600} was

514   adjusted to 2. 135 µL cells were added to 15 µL berberine solution in a black 96-well plate.

515   Berberine accumulation was monitored for 40 min by measurement of the fluorescence at the

516   excitation and emission wavelengths of 365 nm and 540 nm respectively. The experiment was

517   performed in biological triplicates.

Protein expression

The expression of all constructs followed a similar procedure. A single clone of freshly transformed cells was used for inoculation of a pre-culture in LB medium with an appropriate selection antibiotic. The pre-culture was incubated overnight at 37 °C. 1 L medium (LB medium with 1 % glucose for DARPin expression, TB medium for all other constructs) with an appropriate selection antibiotic was inoculated with 10 mL pre-culture and incubated at 37 °C under continuous shaking until an OD_{600} value of 0.5-0.8 was reached. Expression was then induced with 1 mM isopropyl-beta-D-thiogalactopyranosid (IPTG). For expression of DARPin the culture was incubated at 37 °C for 4 h. For all other constructs the expression culture was incubated at 20 °C for 20 h. Cells were then harvested at 17600 g and 4 °C for 20 min. The cell pellet from the expression culture was resuspended in 20 mM Tris-HCl, pH 8.0, 0.5 M NaCl, 2 mM $MgCl_2$, 10 mg/L DNAseI and 0.2 mM PMSF and lysed with a Stansted SPCH-EP-10 pressure cell homogenizer (Homogenizing Systems Ltd, UK) at 22 kPsi. Cell debris in the lysate were removed by centrifugation at 20000 g and 4 °C for 20 min

Purification AcrB and OqxB

The cell lysate prepared as described above was centrifuged at 186000 g and 4 °C for 1 h. The membrane pellet was resuspended in 4 ml 20 mM Tris-HCl pH 8.0, 0.5 M NaCl per g wet membrane weight, frozen in liquid nitrogen and stored at -80 °C until purification. The membrane suspension was diluted with the equal volume of IMAC wash buffer (20 mM Tris pH 7.5, 150 mM NaCl, 10 % (v/v) glycerol) and imidazole was added to a final concentration of 20 mM. n-Dodecyl-β-D-maltopyranoside (DDM) was added to the final concentration of 1 % for solubilisation and the membrane suspension was incubated at 4 °C for 1 h. Insolubilized lipids were removed by centrifugation at 186000 g and 4 °C for 30 min and the detergent extract was incubated with Ni-NTA beads, pre-equilibrated with IMAC wash buffer, for 1 h at 4 °C. The beads were washed three times with 15 column volumes of IMAC wash buffer supplemented with 0.02 % DDM and containing 20 mM, 80 mM and 110 mM imidazole (AcrB) or 20 mM, 60 mM and 80 mM imidazole (OqxB). The sample was eluted with 10 column volumes IMAC wash buffer with 220 mM imidazole and 0.02 % DDM, concentrated with an Amicon 100 Ultra-15 concentrator (100 kDa cutoff) and loaded on a Superose 6 10/300 increase column for size exclusion chromatography (SEC) in 20 mM Tris, pH 7.5, 150 mM NaCl, 0.02 % DDM. All purification steps were performed at 4 °C.

Purification DARPin

The cell lysate prepared as described above was centrifuged at 137000 g and 4 °C for 1 h to remove cell debris and insoluble material. The supernatant was loaded on gravity flow Ni-NTA column pre-equilibrated with wash buffer. The resin was washed with 30 column volumes each of wash buffer (50 mM Tris-HCl pH 7.5, 0.4 M NaCl) containing 0 mM and 20 mM imidazole respectively. The sample was eluted with 10 column volumes wash buffer with 250 mM imidazole and concentrated with an Amicon 100 Ultra-15 concentrator (10 kDa cutoff). During the concentration the buffer was exchanged to 50 mM Tris-HCl pH 7.5, 0.4 M NaCl. The purified DARPin was divided into aliquots, frozen in liquid nitrogen and stored at -80 °C until further usage.

Purification saposinA

The cell lysate prepared as described above was incubated for 10 min at 85 °C and precipitates were removed by centrifugation at 20000 g and 4 °C for 30 min. The supernatant was loaded on gravity flow Ni-NTA column pre-equilibrated with buffer. The resin was washed with 10 column volumes each of wash buffer (20 mM HEPES, pH 7.5, 150 M NaCl) containing 0 mM and 20 mM imidazole respectively. The sample was eluted with 6 column volumes wash buffer with 100 mM imidazole, concentrated with an Amicon 100 Ultra-15 concentrator (3 kDa cutoff) and loaded on a Superose 6 10/300 increase column for SEC in 20 mM HEPES pH 7.5, 150 mM NaCl. Purified saposinA was digested with in-house produced TEV protease overnight at 4 °C to remove the 6x-His tag, then the sample was re-applied on the Ni-NTA resin. The flow-though was collected, concentrated, frozen in liquid nitrogen and stored at -80 °C until further usage.

Reconstitution of AcrB and OqxB in salipro nanodiscs (SP-ND)

E coli total lipids (Avanti polar lipids) were dissolved in chloroform, the solvent was evaporated at a rotational evaporator and the lipid film was dissolved in 50 mM HEPES pH 7.5, 150 mM NaCl (final concentration lipids: 10 mg/mL) by sonification in an ultrasonic bad. The lipid stock was frozen in liquid nitrogen and stored at -80 °C until further usage.

Purified, His-tag cleaved saposinA was mixed with the lipid stock in a molar ratio of saposinA:lipids of 1:10 and the volume of the sample was adjusted to 1 mL with 50 mM sodium acetate, pH 4.8, 150 mM NaCl. The sample was incubated for 20 min at 37 °C and precipitates were removed by centrifugation at 20000 g for 10 min. The buffer was exchanged to 20 mM Tris, pH 7.5, 150 mM NaCl using a Sephadex G-25 gravity flow desalting column. The thus formed SP-ND were added to purified, DDM-solubilised AcrB or OqxB in the molar ratio AcrB/OqxB:saposinA:lipids 1:10:100. The volume of the sample was adjusted with detergent-

22

582   free buffer so that the final DDM concentration is 0.01 %. The sample was dialysed against

583   500 mL detergent-free buffer (20 mM Tris, pH 7.5, 150 mM NaCl) overnight at 4 °C and, after

584   buffer exchange against fresh buffer, for further 3 h at 4 °C. Samples were then concentrated

585   with an Amicon 100 Ultra-15 concentrator (100 kDa cutoff) and loaded on a Superose 6 10/300

586   increase column for SEC in 20 mM Tris, pH 7.5, 150 mM NaCl. SEC fractions containing the

587   SP-ND reconstituted AcrB/OqxB were collected and concentrated to 1.5-3 mg/mL for cryo-EM

588   grids preparation.

589   Crystallisation, X-ray data collection and analysis

590   For crystallisation of AcrB in the presence of DARPins, purified, DDM-solubilised AcrB and

591   DARPins were mixed in the molar ratio of 1:2 and incubated for 20 min at 4 °C. Excess DARPin

592   was removed by SEC in 20 mM Tris pH 7.5, 150 mM NaCl, 0.03 % DDM and samples were

593   concentrated to 10-15 mg/mL. For co-crystallisation with minocycline, the substate was added

594   to the final concentration of 2 mM. Crystals were grown by the hanging drop vapor diffusion

595   method in 24-well plates with 1 mL reservoir solution for 1-2 weeks at 18 °C. Asymmetric

596   V612N crystals (LTO state) were obtained from 50 mM N-(2-acetamido)iminodiacetic acid

597   (ADA) pH 6.6, 5 % (v/v) glycerol, 6-9 % (w/v) polyethylene glycol (PEG) 4000, 110-220 mM

598     $(NH_4)_2SO_4$. Symmetric V612N (TTT state) were obtained from 0.1 M MES pH 6.5, 5.5-20.5 %

599   (v/v) PEG400. Apo V612W crystals were obtained from 0.1 M sodium acetate pH 4.5, 0.1 M

600   NaCl, 0.1 M $MgCl_2$, 20-37.5 % (v/v) PEG400. V612W crystals with minocycline were obtained

601   from 0.1 M MES pH 6.5, 5.5-20.5 % (v/v) PEG400. V612F crystals with minocycline were

602   obtained from 0.1 M sodium acetate pH 4.5, 3-7 % (v/v) PEG200, 15-25 % (v/v) PEG400,

603   0.15 M $MgCl_2$, 0.15 M NaCl. For crystallization of apo V612F in the absence of DARPins,

604   purification and crystallization was carried out with cyclohexyl-n-hexyl-β-D-maltoside as

605   detergent as previously described [11]. Clarithromycin was added to the sample with a final

606   concentration of 1.2 mM prior to crystallisation, but no ligand densities were observed in the

607   structure, thus resulting in an apo structure of AcrB. Crystals were obtained from 0.1 M citrate

608   pH 4.6, 5 % (v/v) PEG400, 16-21 % (v/v) PEG300, 8-11 % (v/v) glycerol. Crystals from the

609   ADA and citrate screens were cryo-protected with 28 % (v/v) glycerol, all other crystals were

610   cryo-protected in 20-30 % (v/v) PEG400. Purified OqxB was prepared as described previously

611   [25]. OqxB crystals were grown by the sitting drop vapour diffusion technique at 25˚C. Protein

612   solution was mixed (1:1) with reservoir solution containing 12% PEG4000, 0.2M $MgCl_2$, 100

613   mM ADA (pH 6.5). Crystals were grown within 1~2 weeks to optimal size (0.3 x 0.3 x 0.5

614   mm^3). The concentration of glycerol was gradually increased to 30% (v/v) by soaking in several

steps for optimal cryo-protection. Crystals were picked up using nylon loops (Hampton Research, CA, USA) for flash-cooling in cold nitrogen gas from a cryostat (Rigaku, Japan).

X-ray diffraction data of AcrB crystals were collected at the beamlines X06SA and X10SA of the Swiss Light Source (Paul Scherrer Institut, Villigen, Switzerland) and P13 of the Deutsches Elektronen Synchrotron (Hamburg, Germany). OqxB data sets were collected at 100K using an EIGER hybrid photon-counting (HPC) pixel-array detector (Dectris, CH) on the BL44XU beamline at SPring-8 (Sayo, Japan).

Diffraction data was processed with XDS [46] and the programs from the Phenix package [47,48]. The crystal structures were solved by the molecular replacement method using MOLREP [49] and Phaser [50]. The AcrB (PDB ID: 4dx5) and OqxB (PDB ID: 7cz9) structures were used as the search models. Automated structure refinement was performed with Refmac [51] and phenix.refine [52]. Model building was performed with Coot [53]. MolProbity [54] was used for structure validation. Data collection and refinement statistics are summarised in tables S6-S9. Figures were generated with ChimeraX [55].

Cryogenic electron microscopy (cryo-EM) sample preparation, data collection and analysis

All cryo-EM samples were applied on glow-discharged R1.2/1.3, 300-mesh Cu holey carbon grids (Quantifoil Micro Tools GmbH) and plunge-frozen in liquid ethane using a Vitrobot Mark IV (Thermo Scientific, Waltham, USA). Samples were vitrified at 100 % humidity and 4 °C after blotting with Whatman papers (grade 595) that were pre-equilibrated in the Vitrobot for 1 h. DDM-solubilised samples were vitrified with nominal blotting force of -25, blotting time of 6-10 s and waiting time of 40 s. SP-ND samples were vitrified with blotting force of -3, blotting time of 4-8 s and waiting time of 40 s.

DDM-solubilised AcrB wildtype (1.5 mg/mL) and V612F (1.8 mg/mL) samples were recorded on a FEI Titan Krios cryo-TEM (Thermo Scientific, Waltham, USA) operating at 300 kV in nanoprobe EFTEM equipped with a K2 summit direct detector (Gatan Inc., Pleasanton, USA) and a post-column energy filter (GIF Quantum SE, Gatan) operating in zero-loss mode with a slit width of 20 eV. Data were recorded using Serial-EM [56] at 105000x magnification (1.05 Å pixel size) with defocus values of -0.8 to -3.5 μm. Dose-fractionated movies were acquired in counting mode with a dose rate of 8 e-/Å2s-1 and 50 e-/Å2 total dose per micrograph.

645 The SP-ND V612F (2.8 µg/mL) dataset was acquired on a Titan Krios cryo-TEM (Thermo
646 Scientific, Waltham, USA) operating at 300 kV equipped with a BioQuantum-K3 imaging filter
647 (Gatan Inc., Pleasanton, USA) and a post-column energy filter (GIF Quantum SE, Gatan)
648 operating in zero-loss mode with a slit width of 20 eV. Data were recorded using Serial-EM [56]
649 at 130000x magnification (0.68 Å pixel size) with defocus values of -0.5 to -3.0 µm. Dose-
650 fractionated movies were acquired in counting mode with a dose rate of 16 e-/Å2s-1 and 60 e-
651 /Å2 total dose per micrograph.

652 DDM-solubilised AcrB V612W (1.9 µg/mL), SP-ND AcrB wildtype (2.5 µg/mL) and OqxB
653 (2.7 µg/mL) datasets were acquired on Titan Krios G3i (Thermo Scientific, Waltham, USA)
654 operating at 300 kV, equipped with a BioQuantum-K3 imaging filter (Gatan Inc., Pleasanton,
655 USA) operated in EFTEM mode with a zero-loss peak slit width of 30 eV. Data were recorded
656 using EPU (Thermo Scientific, Waltham, USA) with nominal magnification 105000x (0.837 Å
657 pixel size) and defocus values of -0.8 to -3.5 µm (V612W) and -0-8 to -2.4 (AcrB wildtype and
658 OqxB). Data were acquired as dose-fractionated movies with 50 e-/Å2s-1 total dose per image,
659 equally distributed over 50 fractions.

660 Cryo-EM data analysis was performed with cryoSPARC [57] and Relion [58]. The general
661 processing pipeline is depicted in figure S6 and the processing of each individual dataset in
662 explained in more details in figures S7-14. In brief, first beam-induced motion correction and
663 CTF estimation were performed. For initial particle picking a blob picker with particle diameter
664 of 100-160 Å was used in cryoSPARC. After ab initio reconstitution a 3D reference was created
665 and used for template-based automated particle picking. In Relion, either approximately 1000
666 particles were picked manually and used to create a 2D reference for template-based picking;
667 or a 3D reference of one of the already processed datasets was directly used for template-based
668 picking. Several iterative rounds of 2D classification were performed to remove false positive
669 picks and poor-quality particles. After 3D map reconstruction, a 3D classification was
670 performed to further cure the dataset of poor-quality particles. CTF refinement, local correction
671 of the beam-induced motion and 3D refinement of the trimeric particles without imposed
672 symmetry were performed. Monomers were extracted from the trimers in Relion utilising the
673 C3 pseudosymmetry through the central axis of AcrB and OqxB as described previously [22]. The
674 3D volumes were processed with C3 symmetry and a C3 symmetry expansion was performed.
675 This triplicates the particles and rotates them along the symmetry axis so that all three
676 monomers of each trimer are aligned at the same position. A soft monomer mask created based
677 on the AcrB (PDB ID: 4dx5) or OqxB (PDB ID: 7cz9) models was used to subtract two of the

25

678 monomers. The resulting monomer volume was subjected to several rounds of 3D classification

679 with a varying number of classes (minimal 3). The goal was to obtain the maximum number of

680 classes with the best resolution. The classification utilised the monomer mask used for the

681 subtraction and a low pass filtered trimer volume as the reference map and was performed

682 without image alignment and with a regularisation parameter T of 15. The 3D classes were

683 refined and the conformational state of each class was determined by comparison with each

684 monomer (L, T and O) of the asymmetric AcrB structure (PDB ID: 4dx5), based on

685 characteristic structural features like the position of the subdomains in the porter domain. A

686 custom MATLAB (The MathWorks Inc., Natick, Massachusetts, USA) script was used to

687 calculate the trimer composition of the sample based on the position of the extracted monomers.

688 Structure models of the best resolved O state monomers of AcrB were build based on the

689 experimental structure of AcrB in the O state (PDB ID: 4dx5). The structure model of OqxB

690 was based on the AlphaFold [59] predicted structure available under Uniprot accession number

691 U5U6L7. Structure refinement was performed with phenix.real_space_refine [52], Coot [53] and

692 ISOLDE [60]. MolProbity [54] was used for structure validation. Data collection and refinement

693 statistics are summarised in the table S10. Figures were generated with ChimeraX [55].

694

695

696

References

1. Darby, E. M. *et al.* Molecular mechanisms of antibiotic resistance revisited. *Nature reviews. Microbiology* **21,** 280–295; 10.1038/s41579-022-00820-y (2023).

2. Ebbensgaard, A. E., Løbner-Olesen, A. & Frimodt-Møller, J. The Role of Efflux Pumps in the Transition from Low-Level to Clinical Antibiotic Resistance. *Antibiotics (Basel, Switzerland)* **9**; 10.3390/antibiotics9120855 (2020).

3. Global burden of bacterial antimicrobial resistance in 2019: a systematic analysis. *Lancet (London, England)* **399,** 629–655; 10.1016/S0140-6736(21)02724-0 (2022).

4. Kobylka, J., Kuth, M. S., Müller, R. T., Geertsma, E. R. & Pos, K. M. AcrB: a mean, keen, drug efflux machine. *Annals of the New York Academy of Sciences* **1459,** 38–68; 10.1111/nyas.14239 (2020).

5. Yamaguchi, A., Nakashima, R. & Sakurai, K. Structural basis of RND-type multidrug exporters. *Frontiers in microbiology* **6,** 327; 10.3389/fmicb.2015.00327 (2015).

6. El Meouche, I. & Dunlop, M. J. Heterogeneity in efflux pump expression predisposes antibiotic-resistant cells to mutation. *Science (New York, N.Y.)* **362,** 686–690; 10.1126/science.aar7981 (2018).

7. Alav, I. *et al.* Structure, Assembly, and Function of Tripartite Efflux and Type 1 Secretion Systems in Gram-Negative Bacteria. *Chemical reviews* **121,** 5479–5596; 10.1021/acs.chemrev.1c00055 (2021).

8. Li, Y., Cross, T. S. & Dörr, T. Analysis of AcrB in Klebsiella pneumoniae reveals natural variants promoting enhanced multidrug resistance. *Research in microbiology* **173,** 103901; 10.1016/j.resmic.2021.103901 (2022).

9. Swick, M. C., Morgan-Linnell, S. K., Carlson, K. M. & Zechiedrich, L. Expression of multidrug efflux pump genes acrAB-tolC, mdfA, and norE in Escherichia coli clinical isolates as a function of fluoroquinolone and multidrug resistance. *Antimicrobial agents and chemotherapy* **55,** 921–924; 10.1128/AAC.00996-10 (2011).

10. Salehi, B., Ghalavand, Z., Yadegar, A. & Eslami, G. Characteristics and diversity of mutations in regulatory genes of resistance-nodulation-cell division efflux pumps in association with drug-resistant clinical isolates of Acinetobacter baumannii. *Antimicrobial resistance and infection control* **10,** 53; 10.1186/s13756-021-00924-9 (2021).

11. Seeger, M. A. *et al.* Structural asymmetry of AcrB trimer suggests a peristaltic pump mechanism. *Science (New York, N.Y.)* **313,** 1295–1298; 10.1126/science.1131542 (2006).

12. Murakami, S., Nakashima, R., Yamashita, E., Matsumoto, T. & Yamaguchi, A. Crystal structures of a multidrug transporter reveal a functionally rotating mechanism. *Nature* **443,** 173–179; 10.1038/nature05076 (2006).

13. Eicher, T. *et al.* Transport of drugs by the multidrug transporter AcrB involves an access and a deep binding pocket that are separated by a switch-loop. *Proceedings of the National Academy of Sciences of the United States of America* **109,** 5687–5692; 10.1073/pnas.1114944109 (2012).

14. Eicher, T. *et al.* Coupling of remote alternating-access transport mechanisms for protons and substrates in the multidrug efflux pump AcrB. *eLife* **3**; 10.7554/eLife.03145 (2014).

27

15. Takatsuka, Y. & Nikaido, H. Covalently linked trimer of the AcrB multidrug efflux pump provides support for the functional rotating mechanism. *Journal of bacteriology* **191,** 1729–1737; 10.1128/JB.01441-08 (2009).

16. Murakami, S., Nakashima, R., Yamashita, E. & Yamaguchi, A. Crystal structure of bacterial multidrug efflux transporter AcrB. *Nature* **419,** 587–593; 10.1038/nature01050 (2002).

17. Sennhauser, G., Amstutz, P., Briand, C., Storchenegger, O. & Grütter, M. G. Drug export pathway of multidrug exporter AcrB revealed by DARPin inhibitors. *PLoS biology* **5,** e7; 10.1371/journal.pbio.0050007 (2007).

18. Pos, K. M. Drug transport mechanism of the AcrB efflux pump. *Biochimica et biophysica acta* **1794,** 782–793; 10.1016/j.bbapap.2008.12.015 (2009).

19. Wang, Z. *et al.* An allosteric transport mechanism for the AcrAB-TolC multidrug efflux pump. *eLife* **6**; 10.7554/eLife.24905 (2017).

20. Tsutsumi, K. *et al.* Structures of the wild-type MexAB-OprM tripartite pump reveal its complex formation and drug efflux mechanism. *Nature communications* **10,** 1520; 10.1038/s41467-019-09463-9 (2019).

21. Su, C.-C. *et al.* Structures and transport dynamics of a Campylobacter jejuni multidrug efflux pump. *Nature communications* **8,** 171; 10.1038/s41467-017-00217-z (2017).

22. Ornik-Cha, A. *et al.* Structural and functional analysis of the promiscuous AcrB and AdeB efflux pumps suggests different drug binding mechanisms. *Nature communications* **12,** 6919; 10.1038/s41467-021-27146-2 (2021).

23. Morgan, C. E. *et al.* Cryoelectron Microscopy Structures of AdeB Illuminate Mechanisms of Simultaneous Binding and Exporting of Substrates. *mBio* **12**; 10.1128/mbio.03690-20 (2021).

24. Kato, T. *et al.* Crystal structures of multidrug efflux transporters from Burkholderia pseudomallei suggest details of transport mechanism. *Proceedings of the National Academy of Sciences of the United States of America* **120,** e2215072120; 10.1073/pnas.2215072120 (2023).

25. Bharatham, N. *et al.* Structure and function relationship of OqxB efflux pump from Klebsiella pneumoniae. *Nature communications* **12,** 5400; 10.1038/s41467-021-25679-0 (2021).

26. Glavier, M. *et al.* Antibiotic export by MexB multidrug efflux transporter is allosterically controlled by a MexA-OprM chaperone-like complex. *Nature communications* **11,** 4948; 10.1038/s41467-020-18770-5 (2020).

27. Leus, I. V., Roberts, S. R., Trinh, A., W Yu, E. & Zgurskaya, H. I. Nonadditive functional interactions between ligand-binding sites of the multidrug efflux pump AdeB from Acinetobacter baumannii. *Journal of bacteriology* **206,** e0021723; 10.1128/jb.00217-23 (2024).

28. Bohnert, J. A., Schuster, S., Fähnrich, E., Trittler, R. & Kern, W. V. Altered spectrum of multidrug resistance associated with a single point mutation in the Escherichia coli RND-type MDR efflux pump YhiV (MdtF). *The Journal of antimicrobial chemotherapy* **59,** 1216–1222; 10.1093/jac/dkl426 (2007).

29. Coyne, S., Rosenfeld, N., Lambert, T., Courvalin, P. & Périchon, B. Overexpression of resistance-nodulation-cell division pump AdeFGH confers multidrug resistance in Acinetobacter baumannii. *Antimicrobial agents and chemotherapy* **54,** 4389–4393; 10.1128/AAC.00155-10 (2010).

28

776 30. Hansen, L. H., Jensen, L. B., Sørensen, H. I. & Sørensen, S. J. Substrate specificity of the OqxAB
777   multidrug resistance pump in Escherichia coli and selected enteric bacteria. *The Journal of*
778   *antimicrobial chemotherapy* **60,** 145–147; 10.1093/jac/dkm167 (2007).

779 31. Köhler, T. *et al.* Characterization of MexE-MexF-OprN, a positively regulated multidrug efflux
780   system of Pseudomonas aeruginosa. *Molecular microbiology* **23,** 345–354; 10.1046/j.1365-
781   2958.1997.2281594.x (1997).

782 32. Su, K., Mayans, O., Diederichs, K. & Fleming, J. R. Pairwise sequence similarity mapping with
783   PaSiMap: Reclassification of immunoglobulin domains from titin as case study. *Computational*
784   *and structural biotechnology journal* **20,** 5409–5419; 10.1016/j.csbj.2022.09.034 (2022).

785 33. Nakashima, R., Sakurai, K. & Yamaguchi, A. *Structures of the multidrug exporter AcrB reveal a*
786   *proximal multisite drug-binding pocket* (2011).

787 34. Zhang, Z., Morgan, C. E., Bonomo, R. A. & Yu, E. W. Cryo-EM Structures of the Klebsiella
788   pneumoniae AcrB Multidrug Efflux Pump. *mBio* **14,** e0065923; 10.1128/mbio.00659-23 (2023).

789 35. Tam, H.-K. *et al.* Allosteric drug transport mechanism of multidrug transporter AcrB. *Nature*
790   *communications* **12,** 3889; 10.1038/s41467-021-24151-3 (2021).

791 36. Frauenfeld, J. *et al.* A saposin-lipoprotein nanoparticle system for membrane proteins. *Nature*
792   *methods* **13,** 345–351; 10.1038/nmeth.3801 (2016).

793 37. Pravda, L. *et al.* MOLEonline: a web-based tool for analyzing channels, tunnels and pores (2018
794   update). *Nucleic acids research* **46,** W368-W373; 10.1093/nar/gky309 (2018).

795 38. Wilhelm, J. & Pos, K. M. Molecular insights into the determinants of substrate specificity and
796   efflux inhibition of the RND efflux pumps AcrB and AdeB. *Microbiology (Reading, England)* **170**;
797   10.1099/mic.0.001438 (2024).

798 39. Zhang, Z. *et al.* Cryo-Electron Microscopy Structures of a Campylobacter Multidrug Efflux Pump
799   Reveal a Novel Mechanism of Drug Recognition and Resistance. *Microbiology spectrum* **11,**
800   e0119723; 10.1128/spectrum.01197-23 (2023).

801 40. Saier, M. H., Tran, C. V. & Barabote, R. D. TCDB: the Transporter Classification Database for
802   membrane transport protein analyses and information. *Nucleic acids research* **34,** D181-6;
803   10.1093/nar/gkj001 (2006).

804 41. Madeira, F. *et al.* Search and sequence analysis tools services from EMBL-EBI in 2022. *Nucleic*
805   *acids research* **50,** W276-9; 10.1093/nar/gkac240 (2022).

806 42. Letunic, I. & Bork, P. Interactive Tree of Life (iTOL) v6: recent updates to the phylogenetic tree
807   display and annotation tool. *Nucleic acids research*; 10.1093/nar/gkae268 (2024).

808 43. Crooks, G. E., Hon, G., Chandonia, J.-M. & Brenner, S. E. WebLogo: a sequence logo generator.
809   *Genome research* **14,** 1188–1190; 10.1101/gr.849004 (2004).

810 44. Pos, K. M. & Diederichs, K. Purification, crystallization and preliminary diffraction studies of AcrB,
811   an inner-membrane multi-drug efflux protein. *Acta crystallographica. Section D, Biological*
812   *crystallography* **58,** 1865–1867; 10.1107/s0907444902013963 (2002).

813 45. Plé, C. *et al.* Pyridylpiperazine-based allosteric inhibitors of RND-type multidrug efflux pumps.
814   *Nature communications* **13,** 115; 10.1038/s41467-021-27726-2 (2022).

815 46. Kabsch, W. XDS. *Acta crystallographica. Section D, Biological crystallography* **66,** 125–132;
816   10.1107/S0907444909047337 (2010).

817   47. Adams, P. D. *et al.* PHENIX: a comprehensive Python-based system for macromolecular structure
818   solution. *Acta crystallographica. Section D, Biological crystallography* **66,** 213–221;
819   10.1107/S0907444909052925 (2010).

820   48. Adams, P. D. *et al.* PHENIX: building new software for automated crystallographic structure
821   determination. *Acta crystallographica. Section D, Biological crystallography* **58,** 1948–1954;
822   10.1107/s0907444902016657 (2002).

823   49. Vagin, A. & Teplyakov, A. MOLREP : an Automated Program for Molecular Replacement. *J Appl*
824   *Crystallogr* **30,** 1022–1025; 10.1107/S0021889897006766 (1997).

825   50. McCoy, A. J. *et al.* Phaser crystallographic software. *J Appl Crystallogr* **40,** 658–674;
826   10.1107/S0021889807021206 (2007).

827   51. Murshudov, G. N., Vagin, A. A. & Dodson, E. J. Refinement of macromolecular structures by the
828   maximum-likelihood method. *Acta crystallographica. Section D, Biological crystallography* **53,**
829   240–255; 10.1107/S0907444996012255 (1997).

830   52. Afonine, P. V. *et al.* Towards automated crystallographic structure refinement with phenix.refine.
831   *Acta crystallographica. Section D, Biological crystallography* **68,** 352–367;
832   10.1107/S0907444912001308 (2012).

833   53. Emsley, P., Lohkamp, B., Scott, W. G. & Cowtan, K. Features and development of Coot. *Acta*
834   *crystallographica. Section D, Biological crystallography* **66,** 486–501;
835   10.1107/S0907444910007493 (2010).

836   54. Chen, V. B. *et al.* MolProbity: all-atom structure validation for macromolecular crystallography.
837   *Acta crystallographica. Section D, Biological crystallography* **66,** 12–21;
838   10.1107/S0907444909042073 (2010).

839   55. Pettersen, E. F. *et al.* UCSF ChimeraX: Structure visualization for researchers, educators, and
840   developers. *Protein science : a publication of the Protein Society* **30,** 70–82; 10.1002/pro.3943
841   (2021).

842   56. Mastronarde, D. N. Automated electron microscope tomography using robust prediction of
843   specimen movements. *Journal of structural biology* **152,** 36–51; 10.1016/j.jsb.2005.07.007
844   (2005).

845   57. Punjani, A., Rubinstein, J. L., Fleet, D. J. & Brubaker, M. A. cryoSPARC: algorithms for rapid
846   unsupervised cryo-EM structure determination. *Nature methods* **14,** 290–296;
847   10.1038/nmeth.4169 (2017).

848   58. Scheres, S. H. W. RELION: implementation of a Bayesian approach to cryo-EM structure
849   determination. *Journal of structural biology* **180,** 519–530; 10.1016/j.jsb.2012.09.006 (2012).

850   59. Jumper, J. *et al.* Highly accurate protein structure prediction with AlphaFold. *Nature* **596,** 583–
851   589; 10.1038/s41586-021-03819-2 (2021).

852   60. Croll, T. I. ISOLDE: a physically realistic environment for model building into low-resolution
853   electron-density maps. *Acta crystallographica. Section D, Structural biology* **74,** 519–530;
854   10.1107/S2059798318002425 (2018).

855